Ocean Engineering 234 (2021) 109279

Contents lists available at ScienceDirect

Ocean Engineering

journal homepage: www.elsevier.com/locate/oceaneng

Hydrodynamic loads on a restrained ROV under waves and current

Roman Gabl [a,*], Thomas Davey [a], Yu Cao [b], Qian Li [b], Boyang Li [b,c], Kyle L. Walker [b], Francesco Giorgio-Serchi [b], Simona Aracri [b,d], Aristides Kiprakis [b], Adam A. Stokes [b], David M. Ingram [a,b]

[a] FloWave Ocean Energy Research Facility, School of Engineering, The University of Edinburgh, Max Born Crescent, Edinburgh EH9 3BF, UK
[b] School of Engineering, The University of Edinburgh, Sanderson Building, Robert Stevenson Road, Edinburgh EH9 3FB, UK
[c] Department of Aeronautical and Aviation Engineering, The Hong Kong Polytechnic University, 11 Yuk Choi Rd, Hung Hom, Kowloon, Hong Kong
[d] Institute for the Study of Anthropic Impacts and Sustainability in Marine Environment (IAS), National Research Council (CNR), Via De Marini 16, Genova 16149, Italy

ARTICLE INFO

Keywords:
Experimental investigation
Fluid–structure-interaction
Hydrodynamic forces
Motion capturing
Offshore operation
ROV
Station keeping
Wave gauges
Wave tank

ABSTRACT

Remotely Operated (underwater) Vehicles (ROV) have a wide range of maritime applications, including repair and maintenance. Quantifying hydrodynamic loads is important for the design and control of these ROVs. A novel approach with eight tethers was used to restrain a commercially available ROV, namely the BlueROV2 (Blue Robotics, Torrance, USA), in the mid depth of the FloWave wave and current test tank. This experimental set-up allowed the measurement of the forces under realistic flow around the ROV without introducing significant interference. The paper presents the analysis of the load cell data as forces and moments in relation to the observed motion and rotation of the ROV. In addition to active propelled cases, a variation of current speed (up to 1 m/s) coming out of the four directions as well as different regular waves were tested. Three different distances of a cylindrical obstacle provided a quantification of the effect of flow shadowing from a structure in front of the ROV. The results can also be used as a validation experiment to expand the application of ROVs and the influence of obstacles based on numerical simulations.

1. Introduction

Utilising ROVs for subsea operations is becoming of growing interest to the offshore energy industry. Recently, there has been substantial research into employing remotely controlled underwater vehicles for repair and maintenance operations across different sectors, including, but not limited to, offshore renewable energy, oil and gas operations and marine sciences (Capocci et al., 2017; Aguirre-Castro et al., 2019; Erena et al., 2019; Khojasteh and Kamali, 2017; Sivčev et al., 2018a,b). Inspection of maritime and offshore assets is conducted periodically through surveys, with ROVs offering a practical solution which is both safe and cost efficient (Christ and Wernli, 2007; Griffiths, 2003). Marine renewable energy plants are typically located in shallow water environments, characterised by strong hydrodynamic forces, which act on the intervention vehicles (Reeve et al., 2004) and make inspection tasks particularly complex (Elvander and Hawkes, 2012). Therefore, in order to simulate the dynamic behaviour of submerged vehicles and develop suitable control methodologies, an accurate hydrodynamic model of the vehicle behaviour is required (Conte et al., 2004; Fossen, 1994). Developing this model requires identification of certain hydrodynamic parameters through either numerical calculations or, more accurately, through experimental procedures.

This paper presents an experimental investigation, which was conducted as part of the ORCA Hub project (Hastie et al., 2018; Sayed et al., 2018) (orcahub.org). Blue Robotics (2020), a commercially available Remotely Operated Vehicle (ROV), was tested under different current and wave conditions. The forces acting on it were measured by eight tethers, which held the ROV at mid water depth in the centre of the circular FloWave Ocean Energy Research Facility at the University of Edinburgh (Draycott et al., 2019; Ingram et al., 2014).

In comparison to other investigations, the experimental setup hereby presented is profoundly different due to the applied usage of the eight tethers to restrain the ROV. Typically a towing tank is utilised, whereby the vehicle is attached to a movable gantry and the gantry is moved at different speeds; this generates forces which act on the underwater vehicle and parameters can be identified through physical measurements (Egeskov et al., 1994; Selvakumar and Asokan, 2012; Obreja and Domnisoru, 2012; Xu et al., 2015). Alternatively, the vehicle can be secured to a bending mechanism and placed within a

* Corresponding author.
E-mail address: Roman.Gabl@ed.ac.uk (R. Gabl).

https://doi.org/10.1016/j.oceaneng.2021.109279
Received 2 July 2020; Accepted 31 May 2021
Available online 10 June 2021

flume, measuring the bending moments through load cells for varying flow rates (Wang and Clark, 2006). Another simpler procedure is the free decay pendulum method, where the vehicle or a scaled model is suspended at one end of a pendulum and the vehicle displaced from an equilibrium position, monitoring the decay of swing amplitude (Eng et al., 2008; Morrison and Yoerger, 1993). Similar experiments have been conducted by allowing the ROV to rotate freely within the flow, monitoring the displacement and inferring parameters (Inoue et al., 2008). Different test classes may result in different identified parameters, which is the focus of the study conducted in Lack et al. (2019). Identified parameters are compared for a towing tank test and an open water self-propelled test; the grapho-analytical method proposed by Mišković et al. (2007) is also explored.

Numerical methods can also be employed to obtain estimations of hydrodynamic parameters and have shown good agreement with experimentally obtained values (Gartner et al., 2018). Another method is to apply Computational Fluid Dynamics (CFD) in simulation, but these results do not account for movements within a non-constant flow (Chin and Lau, 2012; Singh et al., 2017; Yang et al., 2015). Strip theory has also been applied to submerged structures for this purpose and can also be applied to estimate the wave and current induced forces acting on the vehicle (Willy, 2020; Milgram, 2007), but it only applies to slender bodies and therefore would not be an accurate representation for typical work class ROVs. Other studies have focused on more theoretical problems, such as shallow wave forces on submerged thin plates (Roy and Ranjan, 2015; Roy and Ghosh, 2006). For more complex shapes such as the Blue Robotics (2020), numerical calculations can be complex due to its complex, asymmetrical and inherent open-frame structure and hence experimental procedures are preferred, which can provide validation data.

The main aim of the investigation was to provide an experimental set-up, which holds the ROV in place, but minimises disturbances or limitation in the flow directions. FloWave provides a unique facility to deliver current and waves from any direction. This capability could be used by connecting the ROV to a support structure with eight tethers. The current paper presents a summary of the analysis for the forces, moments and six degree of freedom (DoF) motions under current with a flow speed of up to 1 m/s as well as regular waves. Furthermore, an obstacle was placed at three different distances in front of the ROV to quantify flow shadowing effects. The measurements are compared to the forces obtained through self-propelling the ROV. In a very similar approach (Dukan et al., 2011) tested their dynamic positioning system in open waters, not considering the influence of other submerged structures. Additional information and analysis of the experiments are available in Gabl et al. (2020b). The full data-set is freely accessible via the Edinburgh DataShare (Gabl et al., 2020a).

The present document offers the results of a comprehensive set of experiments, encompassing motion control and evaluation of disturbances introduced by currents, waves and surrounding submerged structures. Currently, control algorithms based on classical methods lack the necessary performance to be applicable in a shallow water scenario (Walker et al., 2020a,b). The results can assist in optimising model-based control algorithms for position control of an ROV (Cao et al., 2020) as well as a validation experiment for numerical simulations (Li et al., 2020; Walker et al., 2021), allowing the expansion of the investigation of the shadowing influence.

2. Methodology

2.1. Experimental setup

The experimental investigation presented in this paper was conducted at the FloWave Ocean Energy Research Facility at the University of Edinburgh. A schematic diagram of the facility is shown in Fig. 1. FloWave is a 25 m diameter circular tank, with a total water depth of 2 m. The floor of the tank is buoyant and can be raised out of the water

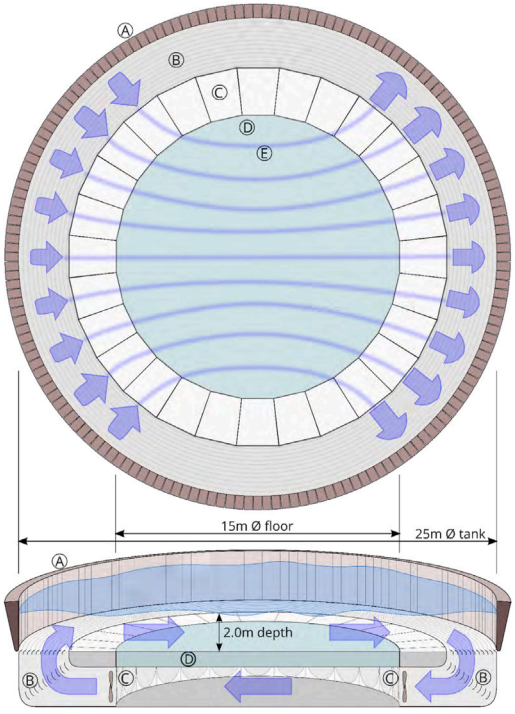

Fig. 1. Schematic diagram of the FloWave circular tank in plan and oblique section showing (A) the wavemakers, (B) the flow turning vanes, (C) the impeller units, (D) the buoyant raisable floor and (E) idealised streamlines of water flow across tank floor (Noble et al., 2015).

for quick model installation and adjustments. Omnidirectional waves are generated by 168 absorbing wavemakers installed on the perimeter of the tank. Water currents are generated by 28 impeller units, installed in the plenum chamber, located under the tank floor. The direction of the flow is controlled by means of turning vanes mounted around the outside of the floor, below and in front of the wavemakers (Ingram et al., 2014). For the presented investigation the current speed was limited to 1 m/s, although the tank could provide over 1.6 m/s if required. Details of the hydraulic boundary conditions are provided in Section 2.3.

The experiments are centred on the commercially available BlueROV2, from Blue Robotics (2020). The ROV was suspended by eight tethers to hold it in place without introducing substantial interference. Therewith it was ensured that the flow around the ROV was as realistic as possible. Fig. 2 shows the experimental set-up on the raised tank floor, including the obstacle in front of the ROV. Further details for the frame can be found in Gabl et al. (2020a,b).

The global coordinate system is defined in the centre of the test tank. A right handed coordinate system was used with the x-axis pointing against the main flow direction and the vertical z-axis orientated downwards. The ROV was suspended in the middle of the test volume with a total water depth of 2 m.

2.2. Instrumentation

Three different systems provided measurements for the presented project: (a) an underwater motion capture system (MoCAP), (b) load cells (LC) and (c) wave gauges (WG), which were only deployed for the cases with waves. A digital pulse provided by the tank was used to synchronise all three different systems.

Six conductive WGs were installed in the main flow and wave direction, which was in this case orthogonal to the movable gantry. Fig. 3 shows the array, which was positioned over the ROV after it was submerged. The accuracy of the WG to measure the elevation of

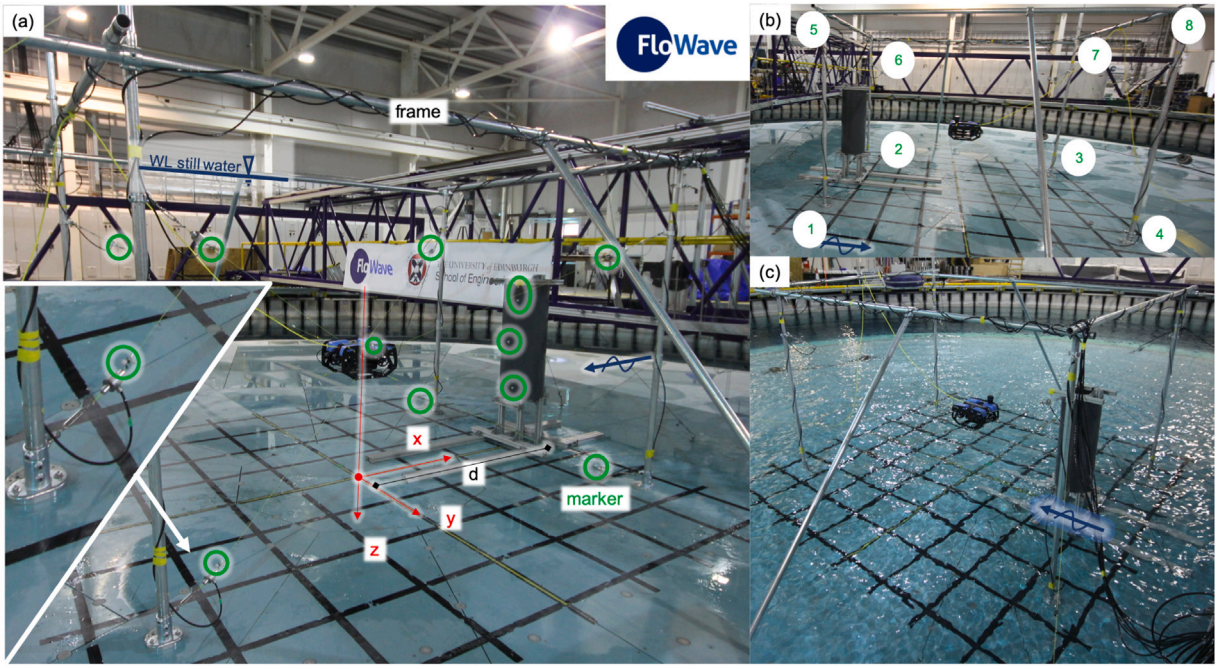

Fig. 2. Experimental set-up in the tank on the raised tank floor with the cylindrical obstacle (a), including a detail view of the connection of one tether with the frame. — (b) numbering of the eight load cells — (c) snapshot of the lowering tank floor before the ROV enters the water.

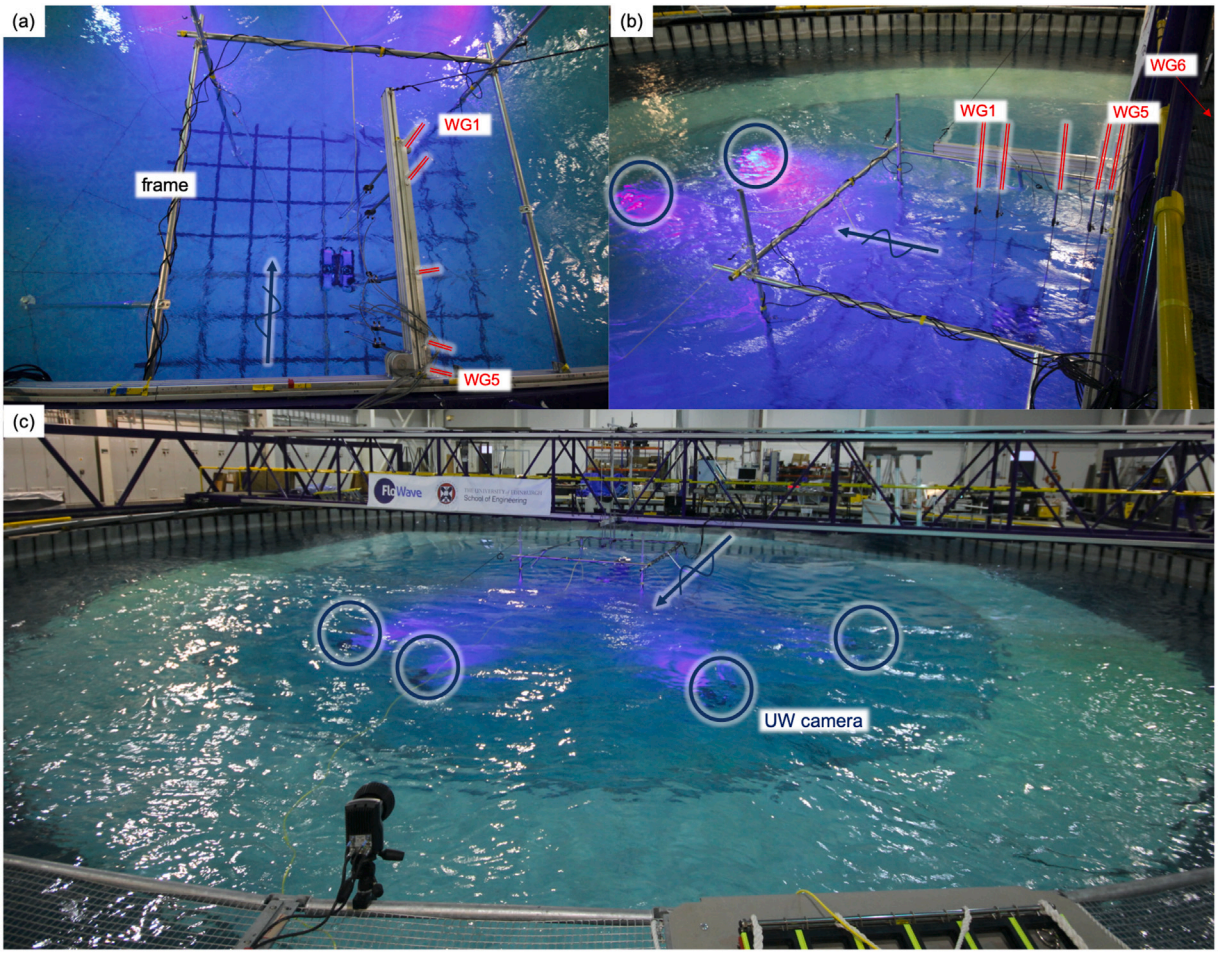

Fig. 3. Submerged experimental set-up in the tank viewed from the gantry (a) top and (b) side view — (c) overview including under water (UW) cameras of the motion capturing system (circled).

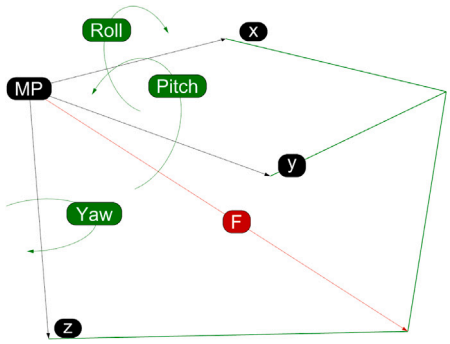

Fig. 4. Definition of the coordinate system and rotations roll, pitch and yaw exemplary shown for one mounting point (MP) and the corresponding measured force F.

the water surface is smaller than or close to 1 mm (Gabl et al., 2018; MARINET, 2020). A daily calibration with 5 points covering ±100 mm was conducted to ensure this high accuracy.

A lightweight Dyneema rope was used to connect the ROV with the support structure constructed from standard 48 mm diameter scaffolding pipes. Each of the tethers included a LC as well as a turnbuckle. This allowed a certain amount of preload to be introduced and precise alignment of the ROV within the support structure on the raised tank floor. This could only be achieved in dry conditions before the complete structure was submerged. Six of the eight used LCs had a rated capacity (RC) of up to 100 N. Two additional ones with a RC of up to 500 N were added because of limited availability of the lower rated type. They were used as LC 7 and 8 (Fig. 2(b)). Both LC types are constructed identically, but, obviously, the ones with a RC of up to 500 N are comparably noisier under lower forces. This is shown in Gabl et al. (2020b). The manufacturers of the LC lists an accuracy smaller than ±0.15% of RC with a typical value of 0.05% (APPLIED MEASUREMENTS Ltd., 2020).

The frame, obstacle (if present) and the ROV were equipped with reflective markers. Some examples are highlighted in Fig. 2(a). They were observed by four underwater cameras of the Qualisys motion capturing system (MoCAP). Fig. 3 presents three pictures of the operating system, which uses blue light to track the markers. At least one daily refinement calibration was conducted to ensure the accuracy of the system was smaller than 1 mm. Seven reflective markers on the ROV were joined together to define a rigid body. The origin of the body coordinate system was defined at the centre of gravity of the ROV and the orientation of the axis was chosen similar to the global coordinate system (Fig. 2). A further eight markers were attached in line with the tether close to the connection point. The connection points of the tether on the ROV were defined as virtual points, which were calculated based on the rigid body. Hence, the working direction of each LC could be identified and also small changes were taken in account. Gabl et al. (2020b) describes the calculation of this vector and how the measured force F is split into the main components for each mounting point (MP).

In addition to the direction of the force F measured by the LC, the main purpose of the MoCAP was to document motion and rotations of the ROV under the hydrodynamic loads. Fig. 4 presents the definitions of roll, pitch and yaw in relation to the axis relative to one exemplary mounting point (MP). All six degree of freedom (DoF) were zeroed by the mean value of the first measurement of the submerged ROV after the initial installation. Consequently, a motion vector (0,0,0) for (X, Y, Z) describes the ideal position in the centre of the tank and in half of the water depth.

2.3. Experimental conditions

The ROV was suspended in the frame at the beginning of the investigation and stayed there throughout the test campaign. The position and preload had to be corrected only one time after extreme loads introduced a change in the system, which was captured in the regular zero measurements (Gabl et al., 2020b). Extended testing was conducted with solely the ROV followed by a number of cases with the cylindrical obstacle in front of the ROV. In Section 3.4, the runs without the obstacle are marked with a distance $d = \infty$ and the additional three distances were 1.7, 1.3 and 0.9 m. The value d describes the distance between the centre of the ROV (aligned with tank centre) and the centre of the cylinder. A step between the chosen distances was identical with the diameter D of the cylindrical obstacle (Gabl et al., 2020b).

To cover an as broad range of operating conditions as possible, a comprehensive set of hydraulic conditions was covered in the experiments, split into cases with and without waves. The cases without waves included a variation of the current speed of up to 1 m/s and different flow directions (discussed in Sections 3.3 and 3.4). The following analysis for the wave conditions focuses on the regular waves, which were chosen with a fixed wave frequency f_W of 0.5 Hz and three different regular wave amplitudes. Except for one series with 0 m/s, all waves were combined with a current speed of 0.4 m/s. The tests were limited to waves with following current approaching the ROV in the main direction (negative x-direction; 180° in the tank definition; Fig. 2). The results of the experiments with regular waves are presented in Section 3.5. A detailed overview of the specific hydraulic conditions for each individual case is presented in Gabl et al. (2020b) and the full data-set is also available (Gabl et al., 2020a).

3. Results

3.1. Overview

This section is split into four parts. Firstly, the cases for which the ROV was active and navigated in different directions are compared in a summary view with the following cases with different hydrodynamic boundary conditions (Section 3.2). Those passive cases are further split to investigate the direction of the current (Section 3.3) as well as the distances of the obstacle in the flow (Section 3.4). In both cases a variation of flow speeds are presented. Section 3.5 focuses on the analysis of the regular waves, which were conducted with a constant flow speed of 0.4 m/s and a variation of the distance d to the obstacle. Further cases can be found in Gabl et al. (2020a,b), which included dynamic motions of the ROV in still water and three irregular waves.

3.2. Comparison of forces and moments due to active ROV and hydrodynamic effects

The first research question is to compare the forces and moments introduced by the active ROV under still water conditions (Fig. 5) to the passive cases. In the latter, current and wave acted on the ROV and caused the measured response (Figs. 6 and 7). The presented figures in this section each include four different analyses and the error bar represents the standard deviation of the full capture time, respectively the repeat time for regular waves. A summary of the total sum of the forces in all three coordinate directions and the resulting moments are provided.

In addition to the total sum for all eight LC, the specific combination of four LC, which measured force components acting in the same relative direction, is added together. These subtotals of each of the opposing sides are shown in a separate graph (for example $F_{x,1,2,5,6}$ present the sum of the x-component for LC1,2,5 and 6). Adding the two sides results in the total sum. It has to be highlighted that the measured forces included a preload, which was equalised for all LC according to Gabl et al. (2020b). This constant offset can vary, but it balances for the total sums. The six degrees of freedom (DoF) are presented separately and zeroed by the mean value of the first measurement of the investigations.

Fig. 5 presents the measurements with an active ROV. All cases were conducted in still water and it was ensured that the ROV provided

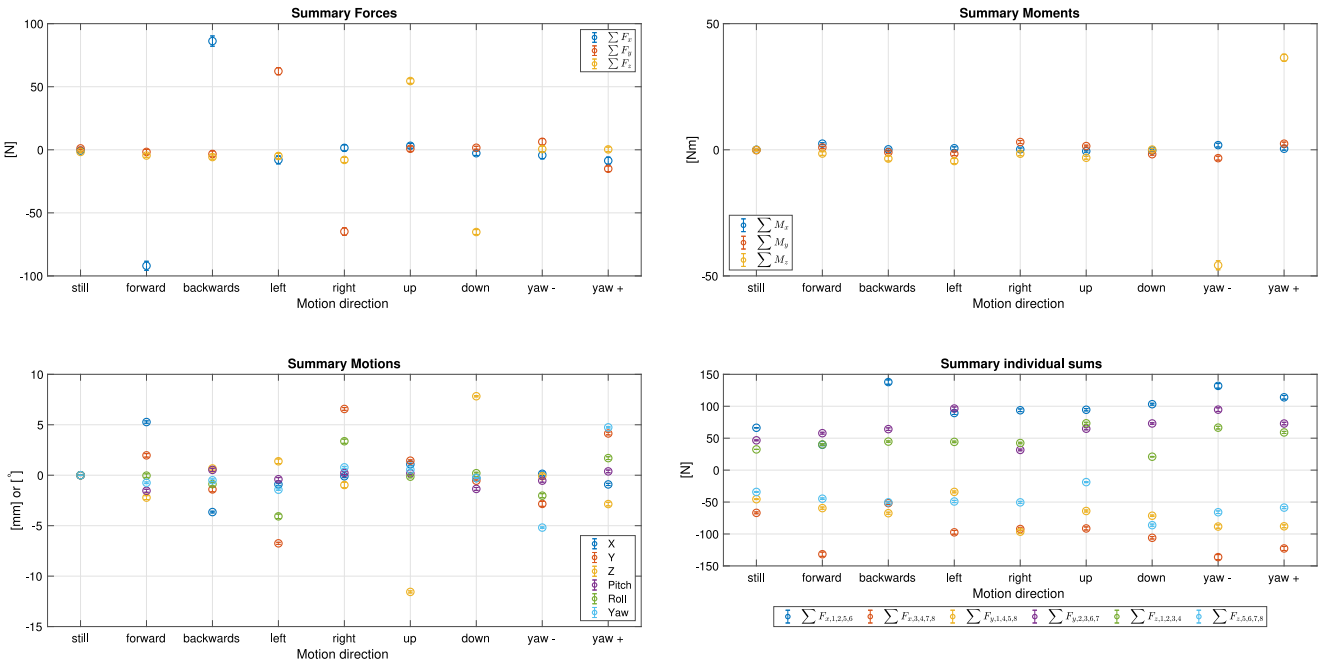

Fig. 5. Summary cases with active ROV.

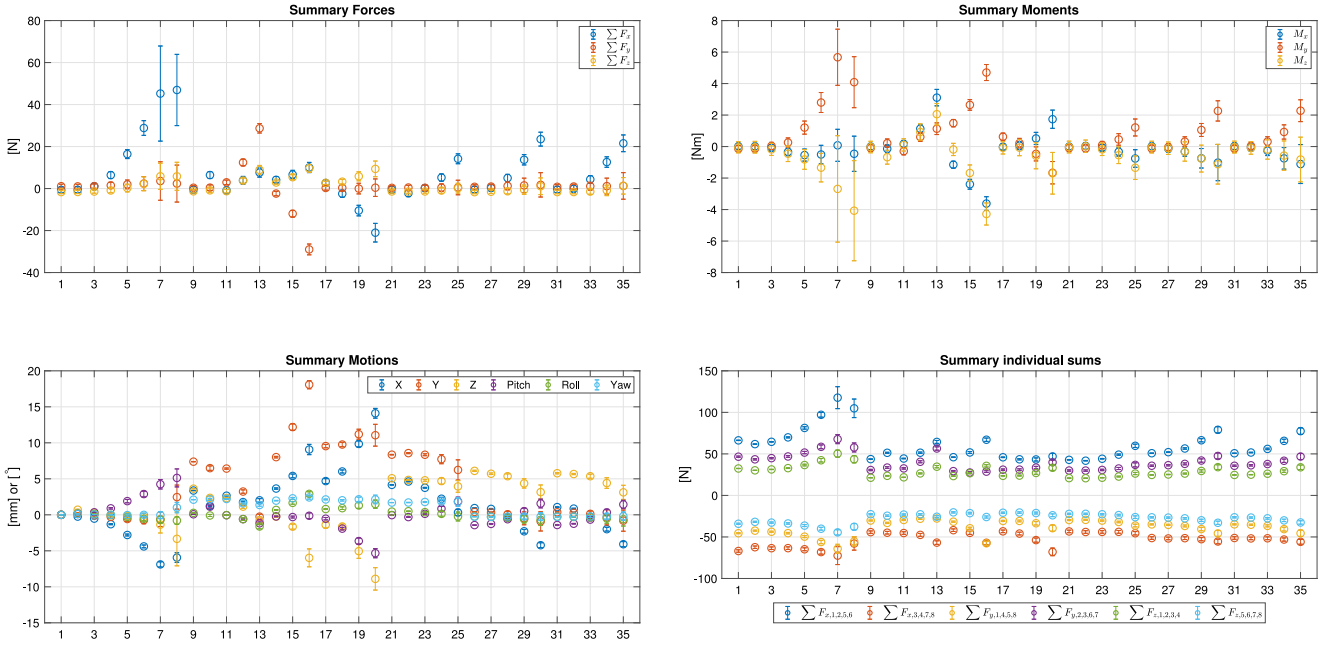

Fig. 6. Summary of cases with current only — hydraulic boundary condition to each number is provided in Gabl et al. (2020b).

a steady force into the system before the measurement was started. After a zero measurement, the ROV was controlled forward, which is equal to the positive x-direction (Fig. 2). The forces follow the same sign convention as the coordinate axis (Fig. 4) and represent the force needed to hold the ROV in place. Hence, a motion in positive directions results in an opposing force in the negative coordinate direction. For the forward motion of the ROV, an average value of −92 N for the sum of F_x could be observed. Only approximately 93 % of this force, namely 86 N, could be reached in the other direction. Left and right resulted in a comparable identical result around 64 N. Slightly higher was the downward force with −65 N. The upwards direction provided a sum of 55 N (85 % of downwards). The two cases with significant moments indicates also a slightly asymmetry of 37 and −46 Nm. The motion also show a certain amount of asymmetry, hence those effects are most likely be caused by imperfections in the tethers and potentially the support structure and less likely by the ROV itself.

The introduced forces and moments by the ROV are larger than all the cases measured under current and wave loads. Fig. 6 provides a summary view of all current only cases, which will be discussed in detail in Section 3.3 and for the obstacle cases in Section 3.4. The similar analysis for the regular waves are presented in Fig. 7. The larger error bars are due to the changing loads caused by the waves. Hence, in Section 3.5 the maximum amplitude spectrum is presented. The increase of the average value after the initial three cases was due to the fact that the following cases were conducted with a flow

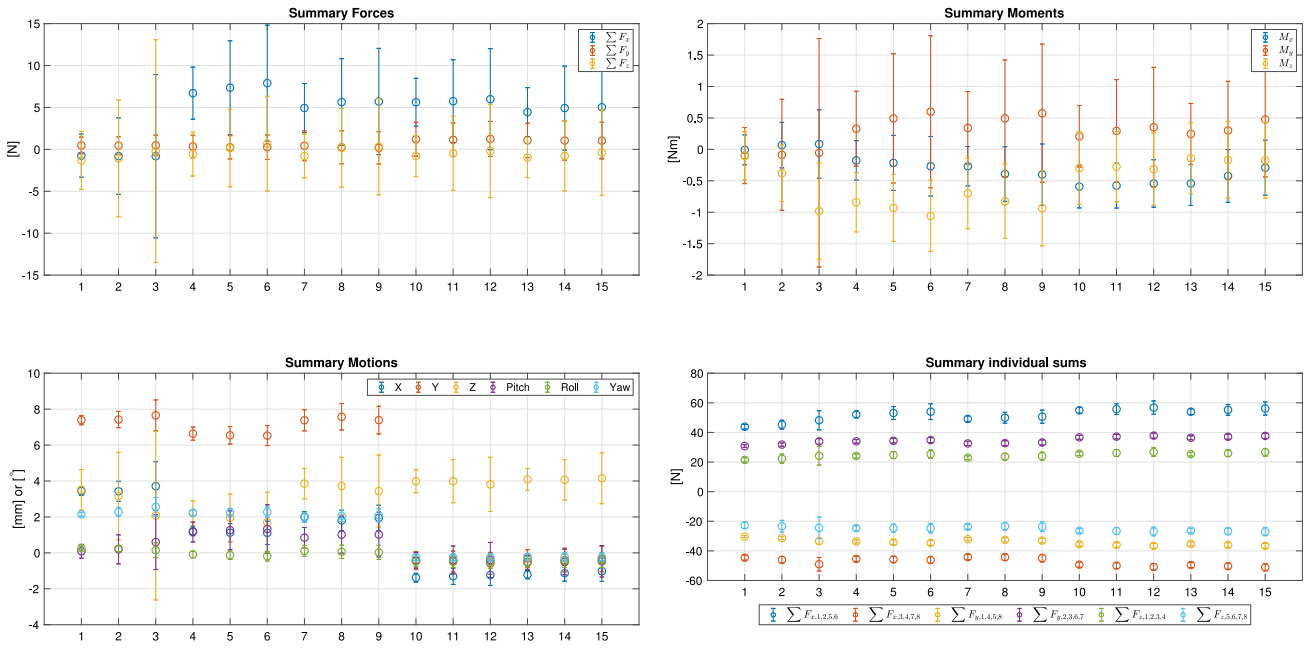

Fig. 7. Summary of regular wave cases including current — hydraulic boundary condition to each number is provided in Gabl et al. (2020b).

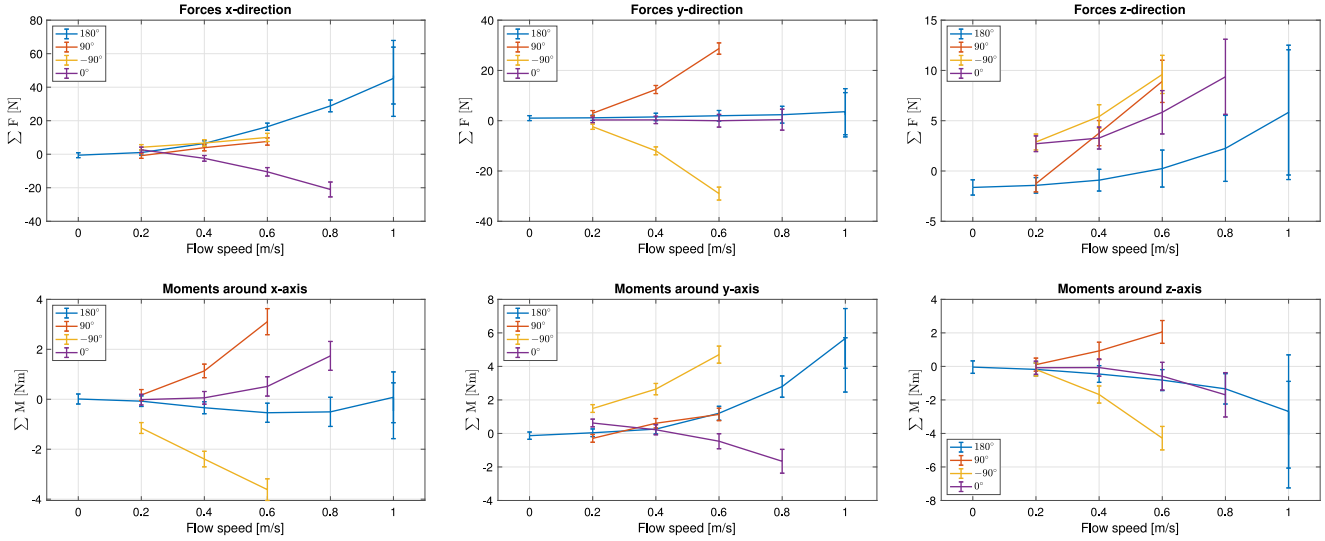

Fig. 8. Current only — variation of current direction and speed — sum of forces and moments in relation to the flow speed.

speed of 0.4 m/s (180°-direction, negative x-direction). All waves were following the current and had a constant frequency of 0.5 Hz.

3.3. Current speed and direction

An overview of the current only cases is provided in Fig. 6 with the detailed hydraulic boundary conditions provided in Gabl et al. (2020b). Those tests were split into two different analysis. In the first step, the direction of the current was in the focus of the testing as well as different flow speeds. Section 3.4 investigates the influence of the obstacle in front of the ROV. Each of the following analyses is presented in two connected figures. The first presents the sum of forces in the three main directions as well as the moments. A second figure shows the observed motions and rotations.

FloWave is a unique wave and current testing facility and provides the capability to deliver current flowing from any direction, as well as waves. The full 360° are split in two half for the commonly used tank definition. One sector reaching from +0 to +180° and the other from −0 to −180°. The boundaries with different signs are identical. For this specific investigation the flow direction from ±180° was defined as the main flow direction (negative x-direction), and unless otherwise stated, this direction is used. Figs. 2 and 3 indicate this direction with a blue arrow. Although the tank could provide the full range of direction, only the three additional main directions were investigated for different flow speeds. The flow from the back is labelled as 0° and pushed the ROV in the positive x-direction. Current from left (−90°, main motion in positive y-direction) and the right side (90°, main motion in negative y-direction) of the ROV were also investigated. Those two side loads are limited to 0.6 m/s and the maximum speed of 1 m/s was only conducted for the 180°. The limiting factor was that high speed flow mobilised massive amount of neutral-buoyant seeding material in the tank, which is normally used for the velocity measurement. As a result the visibility for the underwater motion capturing system decreased significantly and the decision was made not to go up to the full speed of over 1.6 m/s of the tank.

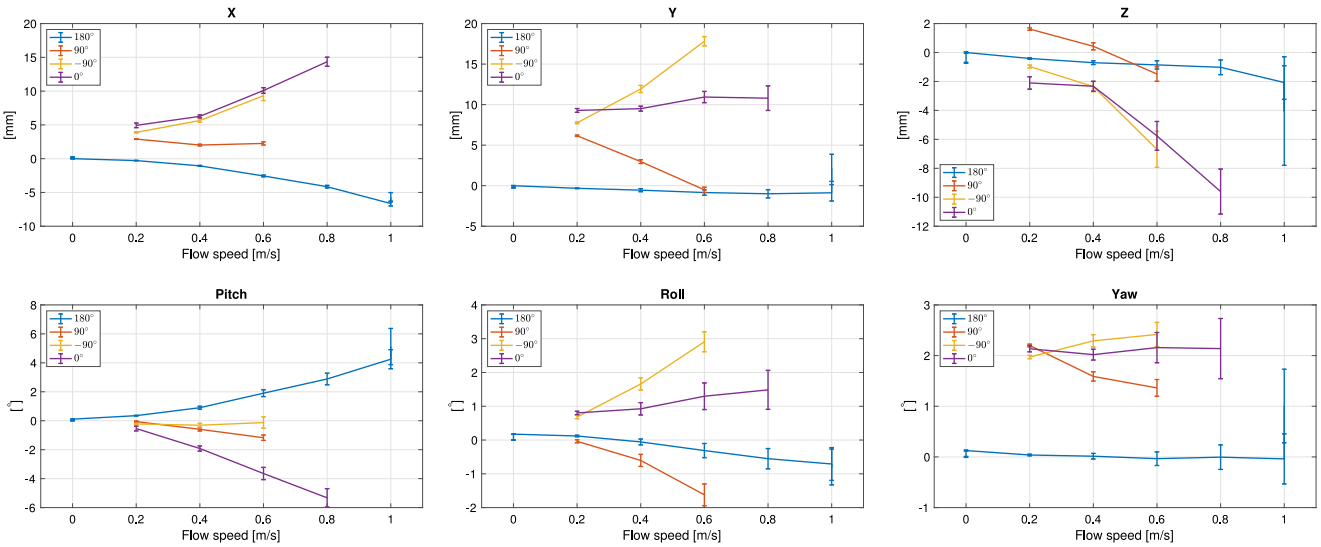

Fig. 9. Current only — variation of current direction and speed — 6 DoF in relation to the flow speed.

Fig. 8 presents the mean values of the sum of forces in the main coordinate directions and the moments. Error bars represent the standard deviation of the full capturing time. As expected, symmetric behaviour could be found for 0° and 180° in $\sum F_x$ and $\sum M_y$ as well as for ±90° in $\sum F_y$ and $\sum M_x$. The moments are not as clear as the forces, hence in all cases an increased flow speed results in an increased $\sum F_z$. This can potentially be caused by slightly different flow conditions over and under the ROV due to its construction. Nevertheless, this vertical component is significantly smaller than the forces in the flow direction. The analysis of the Z-motion, showed in Fig. 9, provides the according motion. With higher speed, the ROV was pushed upwards (negative z-direction). The offsets in the DoF for the other directions in relation to the 180° were caused by bigger loads in the testing program and was corrected later. Details are provided in Gabl et al. (2020b). The decision was made to show this imperfection and not normalise it. Nevertheless, the errors are comparably small and the trends are consistent.

3.4. Obstacle

The following analysis includes the results for 180° direction presented in Section 3.3. They are now marked with a distance ∞ and they represent the cases without an obstacle. Results are presented in relation to the flow speed but for this section the axis of the figures is limited to the 0.8 m/s due to the better visibility.

For this analysis the results in the x-direction are the most important to identify the effect of the shadowing due to the obstacle. The sums of F_x, in Fig. 10, show a consistent reduction of the mean value with a closer obstacle. For the maximum speed 0.8 m/s for this comparison the minimum distance of 0.9 m results in a $\sum F_x$ of 21.5 N, which is approximately 75% of the 28.8 N without the obstacle. The largest reductions in percentage of the initial value without an obstacle could be seen with 0.2 m/s. All cases are presented in Table 1. It has to be mentioned that the small negative $\sum F_x$ is an accepted error after the correction of the load cells and the full data-set is available (Gabl et al., 2020a,b). The shadowing reduces the $\sum F_y$ and $\sum F_z$. Those forces are relatively small and the difference from the case without the obstacle is very small in comparison to the standard deviation of the individual capture times.

Fig. 11 presents the six DoF for this comparison. As mentioned in Section 3.3, those results are zeroed by the first measurement of the investigation after the installation. An offset occurred after investigations with big loads and after the cases with the largest distance d = 1.7 m, the tethers are corrected. Consequently, this case shows a small offset. Nevertheless, the motions and rotations are very small and show a similar behaviour for all distances. Gabl et al. (2020a,b) provides the full data-set.

3.5. Regular waves

As shown in the overview in Fig. 7, the analysis of the loads due to the regular waves have to be adapted. Instead of the previous usage of the full capture time, the repeat time (fully developed wave conditions) are the basis of the following analysis. For each of the twelve time series – three for forces and moments each as well as the six DoF – a FFT analysis was conducted and the maximum value of the amplitude spectrum was identified. These values are reported in Figs. 12 and 13 in relation to the requested wave amplitude a_W (measured values for the amplitude are provide in Gabl et al. (2020b)). The corresponding frequency bins are in nearly all cases identical to the wave frequency of 0.5 Hz. In rare cases, it is half or double, but only for subordinate components, which showed a comparable noisy response in the frequency domain.

Five different experimental configurations were investigated (Figs. 12 and 13). The first set of waves were conducted without current and no obstacle. Those results are marked with "$\infty, 0$". The maximum amplitude was reduced for the following test, which were all conducted with a flow speed of 0.4 m/s. All waves were following the current and hence the measured amplitude is reduced due to the current interaction (Draycott et al., 2018).

The main components of the forces are $\sum F_x$ (in wave direction) as well as $\sum F_z$ (vertical component). Starting with the x-direction and without the obstacle ($d = \infty$), the comparison of with and without current show that the mean value of the forces increases with the current (Fig. 7) and the maximum amplitude spectrum (Fig. 12). By introducing the obstacle in front of the ROV, both parts, namely mean and dynamic value, are reduced. This can be associated with an effect caused by the shadowing of the cylinder. In the vertical direction, the mean value of the $\sum F_z$ is nearly the same for all cases, but the maximum amplitude spectrum show a clear difference between the waves without current $(\infty, 0)$ and the current cases. The results are nearly similar for all distances d including the case without the obstacle. This indicates that the dominating parameter is the wave amplitude, which is reduced by the current interaction. For the requested wave amplitude of 100 mm, the value for $\sum F_z$ is in the range of 5.8 N, which is approximately 60% of 9.8 N for the similar requested wave without current. The measured value of the wave amplitude was 67 mm with

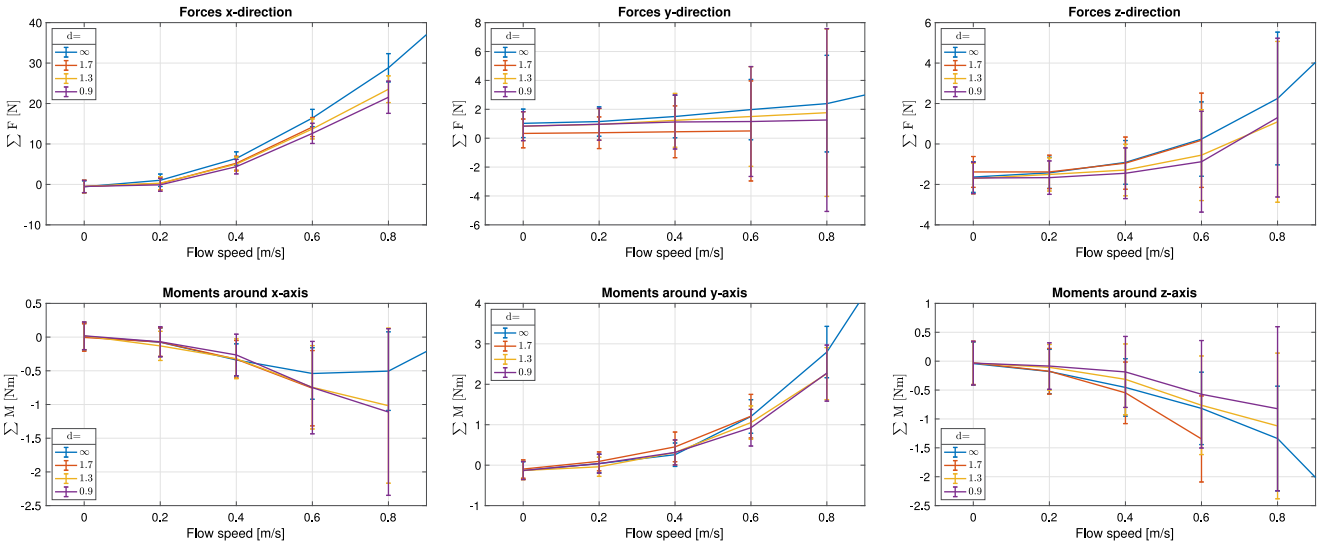

Fig. 10. Current only — variation of the obstacle distance d — sum of forces and moments in relation to the flow speed (limited to 0.8 m/s).

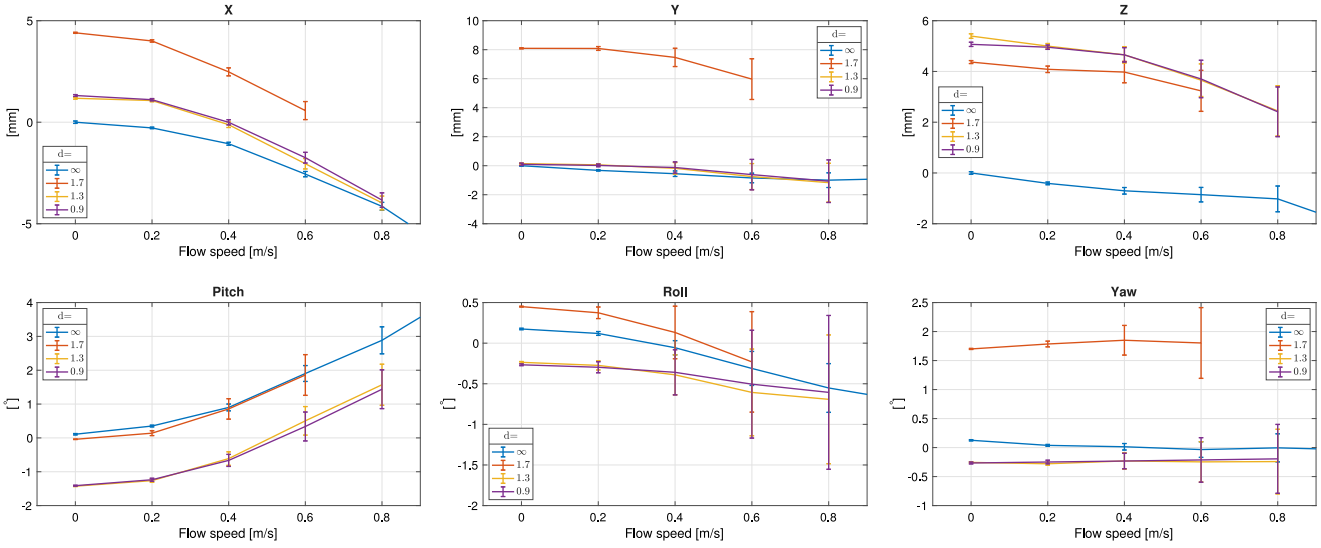

Fig. 11. Current only — variation of the obstacle distance d — 6 DoF in relation to the flow speed (limited to 0.8 m/s).

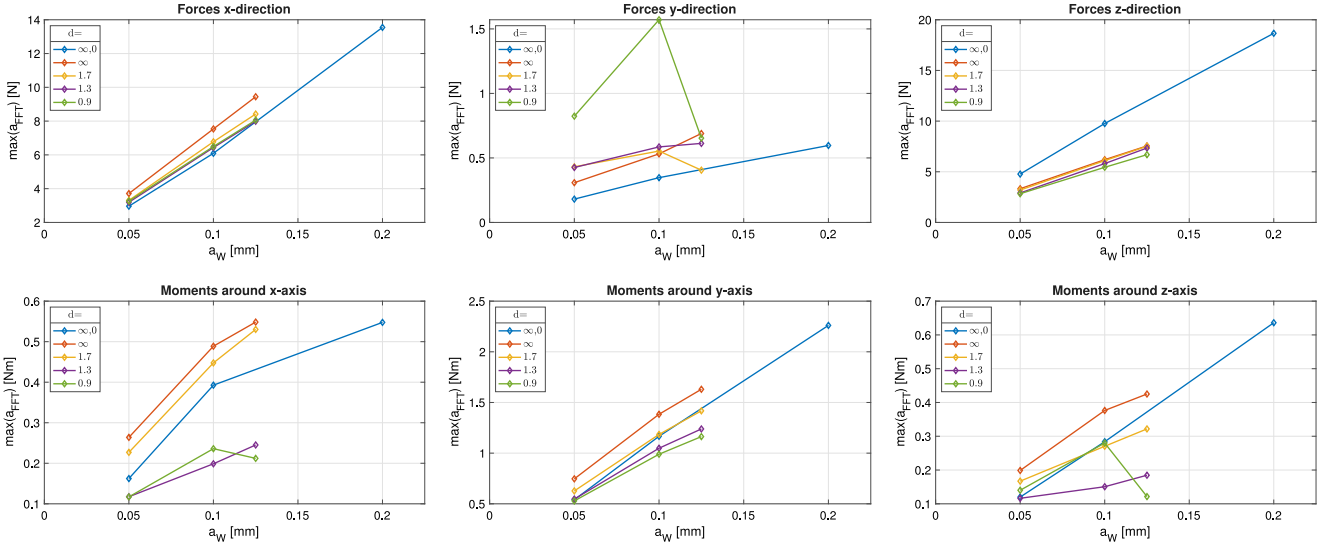

Fig. 12. Regular waves — maximum of the amplitude spectrum $max(a_{FFT})$ for forces and moments in relation to the requested wave amplitude a_W.

Table 1
Comparison mean value of the sums of forces in the x-direction for the cases without an obstacle and the three different distances d depending on the flow speed – comparison with the individual maximum value in % – comparison of the cases with an obstacle to the corresponding case without an obstacle.

Flow speed	$\sum F_x$ [N] for $d=$				$\sum F_x / max(\sum F_x)$ [%]				$\sum F_{x,d} / \sum F_{x,\infty}$ [%]		
[m/s]	∞	1.7	1.3	0.9	∞	1.7	1.3	0.9	1.7	1.3	0.9
0	−0.6	−0.5	−0.5	−0.5	−1%	−4%	−2%	−2%	91%	87%	88%
0.2	1.0	0.2	0.3	−0.1	2%	1%	1%	0%	20%	29%	−10%
0.4	6.4	5.2	5.0	4.4	14%	37%	21%	20%	82%	78%	68%
0.6	16.4	14.2	13.7	12.6	35%	100%	58%	59%	86%	84%	77%
0.8	28.8	–	23.5	21.5	61%	–	100%	100%	–	82%	75%
1	45.2	–	–	–	96%	–	–	–	–	–	–
1	46.9	–	–	–	100%	–	–	–	–	–	–

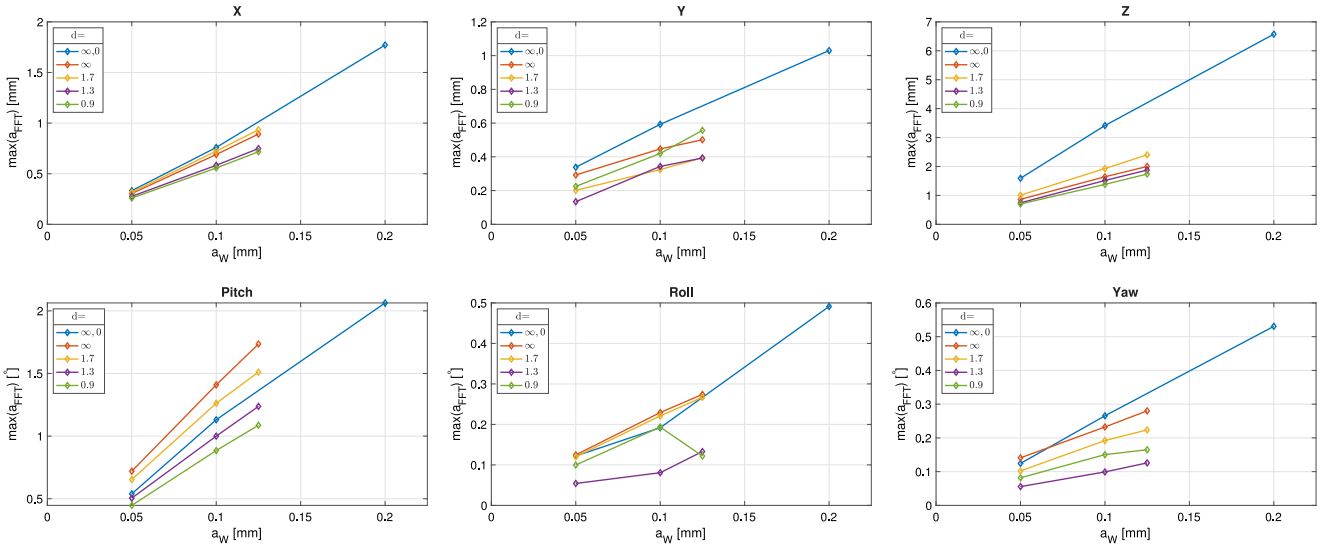

Fig. 13. Regular waves — maximum of the amplitude spectrum $max(a_{FFT})$ for the 6 DoF in relation to the requested wave amplitude a_W.

current, which is approximately 70% of the amplitude of 96 mm for the case without current. Additional investigations are needed with the similar wave amplitudes with and without current to prove this.

The results for $\sum F_y$, $\sum M_x$ and $\sum M_z$ show jumps in the found maximum values, especially for the case with $d = 0.9$ m (Fig. 12). All values are comparably small and the results of the FFT showed significant noise in the frequency domain if an obstacle is present. The sum of moments $\sum M_y$ are calculated based on F_x and F_z and show a clear result. The results for this value go up with the current but decrease consistently with a closer obstacle. Those comparison show an effect of the shadowing of the obstacle.

Fig. 13 presents the corresponding 6 DoF motions for the regular waves. The largest responses could be found in the vertical direction Z for the cases without obstacle and current. All current cases are in the same range. The horizontal responses are all the range of up to 2 mm. For the roll response a similar noisy result was found, which was comparable to and caused by the $\sum F_y$. Pitch and roll indicate both a consistent reduction with a closer obstacle for the cases with current. The motion and rotation analysis underlines the forces and moments presented in Fig. 12.

4. Discussion

Evaluating the overall concept, the frame and the tethers proved to be a good solution and the ROV was held in place with no apparent additional turbulence and shadowing. The measuring instrumentation, namely underwater motion capturing system, load cells (LC) and wave gauges (WG), provided good and consistent results.

An obvious improvement would be to replace the two LC with a rated capacity of up to 500 N with ones which only reach up to 100 N. At the time of the experiments only six were available due to equipment malfunctions. The usage of the two replacement LCs, which are identical in construction but have a higher capacity, had to be accepted.

The neutral-buoyant seeding in the water emerged as a challenge for the underwater motion capture system. Those particles are needed for the velocity measurement and are regularly added to guarantee a high quality acoustic response. At higher velocities more of this material was mobilised into the test volume. This caused rapidly changing visibility in the water and the light settings had to be constantly monitored and adapted. Larger time windows with losses of data had to be accepted only for the highest velocity of 1 m/s. However overall the motion capturing system provided not only a highly accurate measurement of 6 DoF of the ROV under the testing conditions, but it also provided detailed real-time detection of potential vibrations caused by the flow. The frame and the obstacle proved to be very stable, but a slight change in the tether loads and orientation of the ROV could be observed based on the zero measurements. This was highly likely to have been caused by a change in a connection point of the tethers or at a turnbuckle. This occurred after very large loads and was corrected (Gabl et al., 2020b).

In hindsight, the additional use of the upper water motion capturing system, which is also available in FloWave, would be advantageous to provide a check of the position in the dry. For the experiment, this was mainly conducted based on the LC readings controlled by laser measurements, spirit levels as well as the zero measurements in the submerged condition. Furthermore, the above water system would have provided the ability to monitor the motion of the frame, which was surface piercing. It would not have replaced the underwater system but would have had the ability to observe potential vibrations when the flow speed would be further increased. This would have allowed the collection of LC data for higher speeds. For this analysis only data was used for which motion capturing and LC data was available.

Normally, the LC are zeroed regularly, without additional load and under identical hydrostatic conditions. This would require the removal of the ROV and an separate support structure to hold the LC in place. It was decided that the increased uncertainty caused by this procedure was not acceptable. Hence, the ROV was installed and remained in place for the complete investigation. The full zeroing was replaced with regular zero measurements under still water conditions. The key assumption was that all LC should provide the same force and the constant additional buoyancy of the ROV was neglected. Consequently, the aim for the zero measurements was to have a zero value for $\sum F_x$, $\sum F_y$ and $\sum F_z$. This allows to identify the additional forces caused by the hydrodynamic loads on the ROV clearly. Gabl et al. (2020b) describes the analysis and the chosen correction factor.

It was ensured that the umbilical from the ROV did not feed additional loads into the system. Therefore, it was attached to the support structure as visible in Fig. 2. This also ensured that the remaining length of the umbilical from the frame to the control desk had no influence on the ROV.

The obstacle was placed in three different distances from the ROV based on a rail system on the tank floor. A cylinder was used, which can represents a pipeline or a support structure, which has to be investigated by the ROV. As shown in Fig. 2, the pipe was supported by a structure and elevated from the floor. This configuration reduced loads through the structure compared to a full height floor to water surface structure. Nevertheless, these results are mainly used as a validation experiment and the influence of this assumption can be quantified based on the numerical simulation as well as further variations of the diameter and also shape of the obstacle.

The wave cases were limited to a single frequency of 0.5 Hz and current speed of 0.4 m/s (except three runs with 0 m/s). As per Section 3.5, a constant requested wave amplitude was used. The interaction between wave and current resulted in a different measured wave amplitude, which is not ideal to compare the 0 m/s cases with the 0.4 m/s flow conditions. Nevertheless, a good comparison is possible for the four investigated distances d (∞ to 0.9 m) of the obstacle in front of the ROV. The limited boundary conditions were chosen to provide an insight about how waves interact with the ROV. Obviously, an expansion of the investigated wave and current conditions is desirable and it could potentially be part of further testing campaigns.

All investigated flow speeds were based on a previous calibration (Noble et al., 2015) and they have proven to be very accurate, highly reproducible and consistent. The tank produces a realistic turbulence level in the main testing area. The velocity field around the cylinder was not mapped as part of the presented investigation.

5. Conclusion

The paper presents the results of an experimental investigation of a restrained ROV, which was held with eight tethers at mid water depth. This unique experimental set-up enables the investigation of the forces and moments acting on a typical ROV due to waves, current and involves shadowing effects of obstacles. The influence of the supporting structure is minimised and hence those results are valuable as a validation data-set (Gabl et al., 2020b,a) for a wide range of numerical models.

Forces in the tethers, motions and free surface elevations were measured. The first finding was that the ROV could provide 92 N for the forwards and 86 N for the backwards direction, which was larger than all the other recorded sum of forces in any other direction. The comparison of the current flowing in different directions showed a good agreement of the results as well as a direct connection between flow speed and forces, as expected.

Three different distances between the ROV in the tank centre and a cylindrical obstacle in front of the ROV were tested. Shadowing reduced the forces on the ROV significantly in the range of 75% for the smallest distance (0.9 m) and maximum comparable speed of 0.8 m/s. The responses of forces, moments and DoF were found in the same frequency as the waves (0.5 Hz). A closer obstacle reduced the forces in the x and z-directions (wave direction and vertical) as well as in pitch and yaw. The findings are in line with the expectation that a reduction of the forces would be visible. The investigation provides a quantification of the effects of wave, currents and surrounding structures scenarios on the ROV performance. Beside the presented analysis, the full data-set as well as additional analysis are available in Gabl et al. (2020a,b) and can be used as a validation experiment, extending validation and calibration of existing and novel numerical models.

Notation

a	Amplitude waves (mm)
a_W	Amplitude waves (mm) Requested from the wave makers
d	Obstacle distance (m)
D	Diameter of the cylindrical obstacle (m)
f	Frequency wave (Hz)
f_W	Frequency wave (Hz) requested from the wave makers
F	Measured force (N)
F_x, F_y, F_z	Force F split into the main direction (N)
M_x, M_y, M_z	Moments around the main direction (Nm)
x	Distance opposing the main wave direction (m)
X	Motion in x-direction (mm)
y	Distance orthogonal to the main wave direction (m)
Y	Motion in y-direction (mm)
z	Distance vertical direction (m)
Z	Motion in z-direction (mm)
DoF	Degree of freedom
LC	Load cells
MoCAP	Motion capturing system
MP	Mounting point on the ROV
RC	Rated capacity
ROV	Remotely operated (underwater) vehicle
WG	Wave gauge

CRediT authorship contribution statement

Roman Gabl: Conceptualization, Formal analysis, Investigation, Methodology, Writing - original draft. **Thomas Davey:** Conceptualization, Formal analysis, Investigation, Methodology, Writing - original draft. **Yu Cao:** Conceptualization, Investigation, Methodology, Writing - review & editing. **Qian Li:** Investigation, Methodology, Writing - review & editing. **Boyang Li:** Investigation, Methodology, Writing - review & editing. **Kyle L. Walker:** Investigation, Writing - original draft. **Francesco Giorgio-Serchi:** Investigation, Writing - review & editing. **Simona Aracri:** Investigation, Writing - original draft. **Aristides Kiprakis:** Funding acquisition, Writing - review & editing. **Adam A. Stokes:** Funding acquisition, Writing - review & editing. **David M. Ingram:** Funding acquisition, Methodology, Writing - review & editing.

Declaration of competing interest

The authors declare that they have no known competing financial interests or personal relationships that could have appeared to influence the work reported in this paper.

Acknowledgements

This work was funded by the EPSRC project No. EP/R026173/1 , the UK Robotics and Artificial Intelligence Hub for Offshore Energy Asset Integrity Management (ORCA-Hub).

References

Aguirre-Castro, O., Inzunza-González, E., García-Guerrero, E., Tlelo-Cuautle, E., López-Bonilla, O., Olguín-Tiznado, J., Cárdenas-Valdez, J., 2019. Design and construction of an rov for underwater exploration. Sensors 19 (24), http://dx.doi.org/10.3390/s19245387.

APPLIED MEASUREMENTS Ltd., 2020. Submersible Load Cell – DDEN. [Online] Accessed on 30 June 2020. URL: https://appmeas.co.uk/products/load-cells-force-sensors/in-line-submersible-load-cell-dden/.

Blue Robotics, 2020. BlueROV2 Datasheet. June 2016 [Revised Jan. 2019]. [Online] Accessed on 30 June 2020. URL: https://bluerobotics.com/wp-content/uploads/2020/02/br_bluerov2_datasheet_rev6.pdf.

Cao, Y., Li, B., Li, Q., Stokes, A.A., Ingram, D.M., Kiprakis, A., 2020. A nonlinear model predictive controller for remotely operated underwater vehicles with disturbance rejection. IEEE Access 8, 158622–158634. http://dx.doi.org/10.1109/ACCESS.2020.3020530.

Capocci, R., Dooly, G., Omerdić, E., Coleman, J., Newe, T., Toal, D., 2017. Inspection-class remotely operated vehicles – A review. J. Mar. Sci. Eng. 5, http://dx.doi.org/10.3390/jmse5010013.

Chin, C., Lau, M., 2012. Modeling and testing of hydrodynamic damping model for a complex-shaped remotely-operated vehicle for control. J. Mar. Sci. Appl. 11 (2), 150–163. http://dx.doi.org/10.1007/s11804-012-1117-2.

Christ, R., Wernli, R., 2007. The ROV Manual: A User Guide for Observation-Class Remotely Operated Vehicles. http://dx.doi.org/10.1016/B978-0-7506-8148-3.X5000-2.

Conte, G., Zanoli, S.M., Scaradozzi, D., Conti, A., 2004. Evaluation of hydrodynamics parameters of a UUV. A preliminary study. In: First International Symposium on Control, Communications and Signal Processing, Hammamet, Tunisia, 2004. pp. 545–548. http://dx.doi.org/10.1109/ISCCSP.2004.1296437.

Draycott, S., Sellar, B., Davey, T., Noble, D., Venugopal, V., Ingram, D., 2019. Capture and simulation of the ocean environment for offshore renewable energy. Renew. Sustain. Energy Rev. 104, 15–29. http://dx.doi.org/10.1016/j.rser.2019.01.011.

Draycott, S., Steynor, J., Davey, T., Ingram, D., 2018. Isolating incident and reflected wave spectra in the presence of current. Coast. Eng. J. 60 (1), 39–50. http://dx.doi.org/10.1080/05785634.2017.1418798.

Dukan, F., Ludvigsen, M., Sørensen, A., 2011. Dynamic positioning system for a small size ROV with experimental results. In: OCEANS 2011 IEEE - Santander, Spain. http://dx.doi.org/10.1109/Oceans-Spain.2011.6003399.

Egeskov, P., Bjerrum, A., Pascoal, A., Silvestre, C., Aage, C., Smitt, L.W., 1994. Design, construction and hydrodynamic testing of the AUV MARIUS. In: Proceedings of IEEE Symposium on Autonomous Underwater Vehicle Technology (AUV'94), Cambridge, MA, USA. pp. 199–207.

Elvander, J., Hawkes, G., 2012. ROVs and AUVs in support of marine renewable technologies. In: Proc. of Oceans 2012 MTS/IEEE Hampton Roads, VA. http://dx.doi.org/10.1109/OCEANS.2012.6405139.

Eng, Y., Lau, W.S., Low, E., Seet, G., Chin, C.S., 2008. Estimation of the hydrodynamics coefficients of an ROV using free decay pendulum motion. Eng. Lett. 16, 326–331.

Erena, M., Atenza, J., García-Galiano, S., Domínguez, J., Bernabé, J., 2019. Use of drones for the topo-bathymetric monitoring of the reservoirs of the segura river basin. Water 11 (3), http://dx.doi.org/10.3390/w11030445.

Fossen, T., 1994. Guidance and Control of Ocean Vehicles. Wiley.

Gabl, R., Davey, T., Cao, Y., Li, Q., Li, B., Walker, K., Giorgio-Serchi, F., Aracri, S., Kiprakis, A., Stokes, A., Ingram, D., 2020a. Dataset – Experimental Force Data of a Restrained ROV under Waves and Current, [dataset]. University of Edinburgh. Institute for Energy Systems, http://dx.doi.org/10.7488/ds/2835.

Gabl, R., Davey, T., Cao, Y., Li, Q., Li, B., Walker, K., Giorgio-Serchi, F., Aracri, S., Kiprakis, A., Stokes, A., Ingram, D., 2020b. Experimental force data of a restrained ROV under waves and current. Data 5 (3), http://dx.doi.org/10.3390/data5030057.

Gabl, R., Steynor, J., Forehand, D., Davey, T., Bruce, T., Ingram, D., 2018. Capturing the motion of the free surface of a fluid stored within a floating structure. Water (Switzerland) 11 (1), http://dx.doi.org/10.3390/w11010050.

Gartner, N., Richier, M., Hugel, V., 2018. Hydrodynamics parameter identification of submerged bodies: Numerical methods comparison and friction model analysis. In: IEEE International Conference on Intelligent Robots and Systems, Madrid. pp. 5628–5633. http://dx.doi.org/10.1109/IROS.2018.8593770.

Griffiths, G., 2003. The Technology and Applications of Autonomous Underwater Vehicles, Vol. 2. Taylor & Francis, Abingdon, UK, URL: http://eprints.soton.ac.uk/id/eprint/22120.

Hastie, H., Lohan, K., Chantler, M., Robb, D., Ramamoorthy, S., Petrick, R., Vijayakumar, S., Lane, D., 2018. The ORCA hub: Explainable offshore robotics through intelligent interfaces. In: 13th Annual ACM/IEEE International Conference on Human Robot Interaction, Chicago, IL, USA, 5-8, March 2018.

Ingram, D., Wallace, R., Robinson, A., Bryden, I., 2014. The design and commissioning of the first, circular, combined current and wave test basin. In: Oceans 2014 MTS/IEEE Taipei, Taiwan. [131217–002]. IEEE.

Inoue, T., Suzuki, H., Shimamura, T., Nakajima, K., Shioji, G., 2008. Experimental research on horizontal rotation of ROV induced by external forces near sea surface. In: OCEANS 2008, Quebec City, QC. pp. 1–6. http://dx.doi.org/10.1109/OCEANS.2008.5151801.

Khojasteh, D., Kamali, R., 2017. Design and dynamic study of a ROV with application to oil and gas industries of Persian Gulf. Ocean Eng. 136, 18–30. http://dx.doi.org/10.1016/j.oceaneng.2017.03.014.

Lack, S., Rentzow, E., Jeinsch, T., 2019. Experimental parameter identification for an open-frame ROV: Comparison of towing tank tests and open water self-propelled tests. 52, (21), pp. 271–276. http://dx.doi.org/10.1016/j.ifacol.2019.12.319,

Li, Q., Cao, Y., Li, B., Ingram, D.M., Kiprakis, A., 2020. Numerical modelling and experimental testing of the hydrodynamic characteristics for an open-frame remotely operated vehicle. Journal of Marine Science and Engineering (ISSN: 2077-1312) 8 (9), 688. http://dx.doi.org/10.3390/jmse8090688, https://www.mdpi.com/2077-1312/8/9/688.

MARINET, 2020. Work Package 2: Standards and Best Practice – D2.1 Wave Instrumentation Database. Revision: 05. [Online] Accessed on 30 June 2020. URL: http://www.marinet2.eu/wp-content/uploads/2017/04/D2.01-Wave-Instrumentation-Database.pdf.

Milgram, J., 2007. Strip theory for underwater vehicles in water of finite depth. J. Eng. Math. 58 (1–4), 31–50. http://dx.doi.org/10.1007/s10665-006-9101-y.

Mišković, N., Vukić, Z., Barišić, M., 2007. Transfer function identification by using self-oscillations. In: 2007 Mediterranean Conference on Control and Automation, MED, Athens. http://dx.doi.org/10.1109/MED.2007.4433840.

Morrison, A.T., Yoerger, D.R., 1993. Determination of the hydrodynamic parameters of an underwater vehicle during small scale, nonuniform, 1-dimensional translation. In: Proceedings of OCEANS '93, Victoria, BC, Canada, Vol. 2. pp. II277–II282. http://dx.doi.org/10.1109/OCEANS.1993.326105.

Noble, D., Davey, T., Smith, H., Panagiotis, K., Robinson, A., Bruce, T., 2015. Spatial variation of currents generated in the FloWave ocean energy research facility. In: Proceedings of the 11th European Wave and Tidal Energy Conference (EWTEC2015).

Obreja, D., Domnisoru, L., 2012. Theoretical and experimental investigation on the total resistance of an underwater ROV remotely operating vehicle. In: Sustainable Maritime Transportation and Exploitation of Sea Resources – Rizzuto & Guedes Soares.

Reeve, D., Chadwick, A., Fleming, C., 2004. Coastal Engineering: Processes, Theory and Design Practice. Spon Press.

Roy, P., Ghosh, S., 2006. Wave force on vertically submerged circular thin plate in shallow water. Ocean Eng. 33 (14–15), 1935–1953. http://dx.doi.org/10.1016/j.oceaneng.2005.09.010.

Roy, P.D., Ranjan, R., 2015. Variation of wave force on submerged object at shallow water: Fourier series technique. Aquat. Procedia 4, 95–102. http://dx.doi.org/10.1016/j.aqpro.2015.02.014, INTERNATIONAL CONFERENCE ON WATER RESOURCES, COASTAL AND OCEAN ENGINEERING (ICWRCOE'15).

Sayed, M., Nemitz, M., Aracri, S., McConnell, A., McKenzie, R., Stokes, A., 2018. The limpet: A ROS-enabled multi-sensing platform for the ORCA hub. Sensor 18 (10), http://dx.doi.org/10.3390/s18103487.

Selvakumar, J.M., Asokan, T., 2012. A novel approach to measure under water vehicle disturbance force for station keeping control. In: Proceedings of the 9th International Conference on Informatics in Control, Automation and Robotics - Volume 2: ICINCO. INSTICC. SciTePress, pp. 460–463. http://dx.doi.org/10.5220/0004036704600463.

Singh, Y., Bhattacharyya, S., Idichandy, V., 2017. CFD approach to modelling, hydrodynamic analysis and motion characteristics of a laboratory underwater glider with experimental results. J. Ocean Eng. Sci. 2 (2), 90–119. http://dx.doi.org/10.1016/j.joes.2017.03.003.

Sivčev, S., Omerdić, E., Dooly, G., Coleman, J., Toal, D., 2018a. Towards inspection of marine energy devices using ROVs: Floating wind turbine motion replication. Adv. Intell. Syst. Comput. 693, 196–211. http://dx.doi.org/10.1007/978-3-319-70833-1_17.

Sivčev, S., Rossi, M., Coleman, J., Omerdić, E., Dooly, G., Toal, D., 2018b. Collision detection for underwater ROV manipulator systems. Sensors 18 (4), http://dx.doi.org/10.3390/s18041117.

Walker, K.L., Gabl, R., Aracri, S., Cao, Y., Stokes, A.A., Kiprakis, A., Giorgio-Serchi, F., 2021. Experimental validation of wave induced disturbances for predictive station keeping of a remotely operated vehicle. IEEE Robotics and Automation Letters 6 (3), 5421–5428. http://dx.doi.org/10.1109/LRA.2021.3075662.

Walker, K.L., Stokes, A.A., Kiprakis, A., Giorgio-Serchi, F., 2020a. Impact of thruster dynamics on the feasibility of ROV station keeping in waves. In: OCEANS 2020 MTS/IEEE, Singapore.

Walker, K.L., Stokes, A.A., Kiprakis, A., Giorgio-Serchi, F., 2020b. Investigating PID control for station keeping ROVs. In: UKRAS20 Conference: "Robots Into the Real World" Proceedings, Lincoln, UK. pp. 51–53.

Wang, W., Clark, C., 2006. Modeling and Simulation of the VideoRay Pro III Underwater Vehicle. http://dx.doi.org/10.1109/OCEANSAP.2006.4393862.

Willy, C., 2020. Attitude Control of an Underwater Vehicle Subjected to Waves [Master Thesis]. IT and Woods Hole Oceanographic Inst., Cambridge, MA, 1994. URL: http://hdl.handle.net/10945/25706.

Xu, S., Han, D., Ma, Q., 2015. Hydrodynamic forces and moments acting on a remotely operate vehicle with an asymmetric shape moving in a vertical plane. Eur. J. Mech. B 54, 1–9. http://dx.doi.org/10.1016/j.euromechflu.2015.05.007.

Yang, R., Clement, B., Mansour, A., Li, M., Wu, N., 2015. Modeling of a complex-shaped underwater vehicle for robust control scheme. J. Intell. Robot. Syst., Theory Appl. 80 (3–4), 491–506. http://dx.doi.org/10.1007/s10846-015-0186-2.